ADVANCED FUNCTIONAL MATERIALS
www.afm-journal.de

Highly Electron Transparent Graphene for Field Emission Triode Gates

Chi Li, Matthew T. Cole, Wei Lei,* Ke Qu, Kai Ying, Yan Zhang, Alex R. Robertson, Jamie H. Warner, Shuyi Ding, Xiaobing Zhang, Baoping Wang, and William I. Milne**

The enhanced emission performance of a graphene/Mo hybrid gate electrode integrated into a nanocarbon field emission micro-triode electron source is presented. Highly electron transparent gate electrodes are fabricated from chemical vapor deposited bilayer graphene transferred to Mo grids with experimental and simulated data, showing that liberated electrons efficiently traverse multi-layer graphene membranes with transparencies in excess of 50–68%. The graphene hybrid gates are shown to reduce the gate driving voltage by 1.1 kV, whilst increasing the electron transmission efficiency of the gate electrode significantly. Integrated intensity maps show that the electron beam angular dispersion is dramatically improved (87.9°) coupled with a 63% reduction in beam diameter. Impressive temporal stability is noted (<1.0%) with surprising negligible long-term damage to the graphene. A 34% increase in triode perveance and an amplification factor 7.6 times that of conventional refractory metal grid gate electrode-based triodes are noted, thus demonstrating the excellent stability and suitability of graphene gates in micro-triode electron sources.

1. Introduction

Field emission electron sources[1–3] are widely employed in health care and border control technologies and are critical elements in displays,[4] X-ray sources,[5,6] and communications devices such as travelling wave tubes[7] and microwave amplifiers.[8] To date, primarily due to their simplicity, diode-type field emitters have been widely adopted. However, such geometries cannot finely modulate the electron beam current and the rapid modulation of high voltages has proven to be particularly challenging. In diode setups, the magnitude of the emission current is determined either by regulating the high voltage power supply, through the use of complex and often bulky electronics, which unavoidably adjusts the landing energy of the liberated electrons, or by adjusting the inter-electrode gap which requires cumbersome mechanical controls. The addition of an inter-cavity, gate electrode, to create a triode configuration, allows accurate and rapid control over the emission current without such restraints. Since the gate-cathode separation is much less than that of the anode-cathode, triode arrangements permit comparatively small gate biases (typically < 0.5 kV) to exert significant control over the emitted current, thereby offering one possible route toward miniaturization and the development of truly portable field emission electron sources. Nevertheless, it is critical that the electron transmission of the gate be very large in order to reduce leakage and increase performance. The most commonly adopted approach here is to use widely pitched metallic grids as the gate electrode.[9,10] However, if the grid pitch is overly large the gate field-effect is significantly reduced, for a given gate voltage, and the functionality is thus compromised. Conversely, if the pitch is too low then the electron transmission efficiency is reduced, resulting in unacceptably low anode currents. A low-pitch, yet electron transparent gate is evidently desirable.

Herein, we present a hybrid gate structure based on electron transparent free-standing graphene, integrated into a nanocarbon triode field emission electron source. Owing to its outstanding optoelectronic, mechanical, and chemical properties, graphene has been found to be attractive for many applications, from field effect transistors,[11,12] to flexible transparent electrodes,[13,14] and display devices.[13,15–18] Graphene, however, is perhaps best suited for applications requiring transparent conductive electrodes where high transparency across a broad energy range and low sheet resistance, which ensures negligible parasitic charging, low RC time constants, and high bandwidth pulsed operation, are essential.[19–23] Graphene, a single

Dr. C. Li, Prof. W. Lei, Dr. K. Qu, Dr. S. Y. Ding, Prof. X. B. Zhang, Prof. B. P. Wang
Display Research Centre
School of Electronic Science and Engineering
Southeast University
Nanjing, 210096, P. R. China
E-mail: lw@seu.edu.cn

Dr. M. T. Cole, K. Ying, Dr. Y. Zhang, Prof. W. I. Milne
Department of Engineering
Electrical Engineering Division
University of Cambridge
9 JJ Thomson Avenue, CB3 0FA, UK
E-mail: mtc35@cam.ac.uk

Dr A. R. Robertson, Dr. J. H. Warner
Department of Materials
University of Oxford
Parks Road, Oxford, OX1 3PH, UK

Dr. Y. Zhang
Nanjing Camray Technology Ltd, Nanjing Economic & Technological Development Zone, Nanjing, 210000, P. R. China

Prof. W. I. Milne
Department of Information Display
Kyung Hee University
Seoul, 130701, Republic of Korea

DOI: 10.1002/adfm.201300322

atom thick two-dimensional crystalline lattice of hexagonally arranged hybridized sp^2-bonded carbon atoms, can be transferred to and, with recent advances in chemical vapor deposition, grown on arbitrary substrates with relative ease.[24] Though graphene derivatives have shown excellent electron transparency and resilience toward high energy electron beams,[25] the suppression of secondary electron and backscattered emission is critical to ensure high beam currents and negligible loses. Graphitic nanocarbons, and graphene in particular, are low-Z materials and have one of the lowest secondary electron and backscattered electron yields reported to date which, in the case of graphene, is a consequence of its linear dispersion. Subsequently, graphitic nanocarbons are near ideal electron emitters and electron transparent media.[26] To the best of the authors' knowledge, no studies have hitherto considered the use of graphene as a gate electrode material.

In this work, we have investigated the electron transparency of chemical vapor deposited graphene and its functionality as a gate electrode in a nanocarbon triode field emission electron source. We show that, for typical triode operating conditions, our hybrid graphene gates have measured electron transmission efficiencies between 50–70%, some 30–50% higher than traditional metal grid gates, with the graphene presenting an effective transmission efficiency of 97.1%. We reveal a reduction in triode driving voltages which we rationalize by an increase in uniformity in the gate electric field distribution. We also report on the positively augmented profile of the emergent electron beam that shows an angular dispersion of 87.9° (ideal case =90°): a measured improvement of some 12.3° relative to the uncoated gates, coupled with a measured 63% reduction in beam diameter, both of which make our graphene hybrid gates well-suited for micro-focus applications. Finally, we empirically detail the electron beam resilience of our graphene, confirmed over many-hour lifetime tests, whilst demonstrating the excellent temporal stability (<1% variation) of our graphene gate nanocarbon triodes.

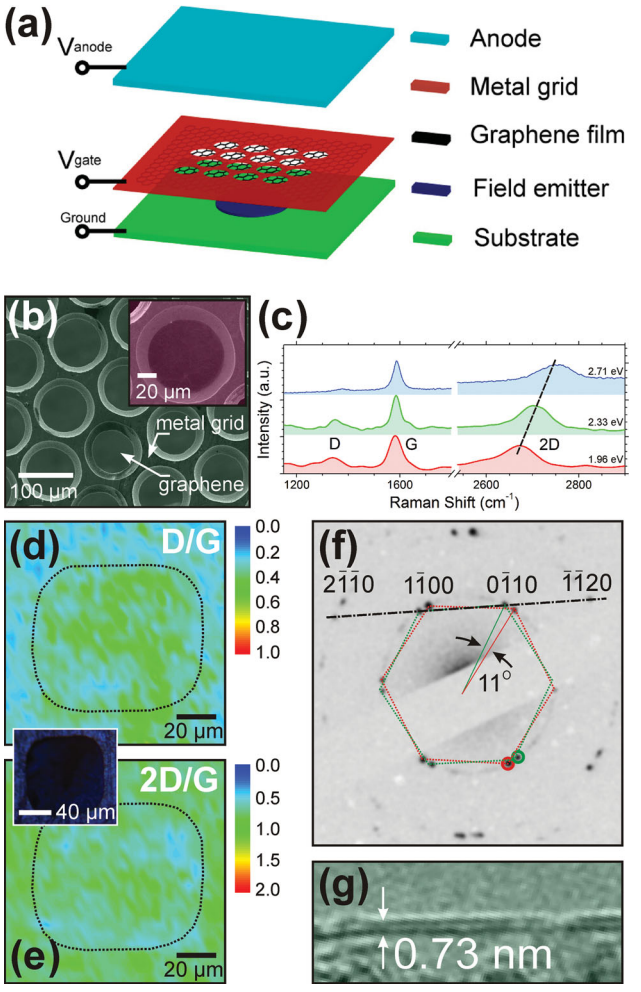

Figure 1. a) Schematic illustration of the nanocarbon field emission triode structure depicting the phosphor/ITO/glass anode (biased at V_a), the graphene hybrid gate electrode (biased at V_g), and a grounded carbon nanotube field emitting cathode. b) Scanning electron image of a typical hybrid gate electrode (scale bar: 100 μm). Insert: Magnified scanning electron micrograph of a single aperture showing complete coverage (scale bar: 20 μm). c) 1.96 eV (red), 2.33 eV (green), 2.71 eV (blue) Raman spectra showing crystalline ($\langle I_D/I_G \rangle = 0.20 \pm 0.16$, $\langle \Gamma_{2D} \rangle = 66.6 \pm 1.5$ cm^{-1}) nominally bilayer layer graphene ($\langle I_{2D}/I_G \rangle = 0.75 \pm 0.10$). Spatially resolved 2.33 eV Raman spectra of a rectangular-grid supported bilayer graphene showing d) I_D/I_G ($\langle I_D/I_G \rangle = 0.30 \pm 0.08$) and e) I_{2D}/I_G ($\langle I_{2D}/I_G \rangle = 0.75 \pm 0.29$) (scale bar: 20 μm). Note that transfer to circular apertures was found to be more reproducible and as such were employed herein. Insert: Optical image of a single aperture (scale bar: 40 μm). f) A typical select area electron diffraction pattern showing turbostratic bilayer graphene with an inter-plane rotation of 11°. g) Cross-section high resolution transmission electron image showing bilayer graphene with a thickness of 0.73 nm.

2. Results and Discussion

2.1. Graphene Gate Characterization

Figure 1a illustrates the structure of the graphene gate hybrid nanocarbon triode. Graphene was synthesized by chemical vapor deposition (CVD) and transferred using poly-methyl methacrylate (PMMA), as described in detail elsewhere, to laser-patterned Mo grids (see Experimental Section).[22] Typical scanning electron images of a fabricated gate are shown in Figures 1b. PMMA-mediated transfer did not degrade the graphene, as determined by Raman spectroscopy (2.71 eV) before and after transfer. The Mo support was critical to ensure structural rigidity of the gate. The effective macroscopic sheet resistance of the Mo/graphene hybrid was also very low (hundreds of Ω sq^{-1}) compared to the as-grown graphene (kΩ sq^{-1}). An electric field screening length of 1.2 nm has been suggested in graphite.[27] Graphitic membranes thinner than this (approximately 3–4 graphene layers) permit a uniform electric field distribution whilst maintain continuity across the individual apertures. In this study, a bilayer material was opted for due to its reduced sheet resistance, relative to our monolayer films, whilst simultaneously offering a thickness less than the critical screening length. The hybrid gate exploits the concurrent high electrical conductivity and electron transparency of the graphene. High electrical conductivity minimized potential drops across individual apertures. This reduces the inter-cavity

Adv. Funct. Mater. 2013,
DOI: 10.1002/adfm.201300322

gate-cathode RC time constant, where R denotes the graphene sheet resistance, thereby facilitating high bandwidth operation. The increase in uniformity of the gate electrodes electric field distribution manifests as a reduction in triode turn-on voltage, a highly collimated electron beam with uniform spread, and extremely stable emission in a miniaturized nanocarbon triode that is inexpensive and well-suited for applications such as portable micro-spot X-ray sources.

To elucidate the electron transparency of the CVD graphene, and the consequent functionality of the nanocarbon field emission triode, a detailed understanding of the material properties of the graphene is critical. UV-Vis transmission spectroscopy measurements (performed on quartz-supported graphene) showed a 550 nm transparency of ≈4.5%, signifying bilayer material.[23,28] Figure 1c shows typical polychromatic Raman spectra acquired at 2.71 eV, 2.33 eV, and 1.96 eV for a CVD graphene sample supported on rectangular-aperture TEM grids. The position and blue-shift dispersion behaviour of the 2D-peak (≈2675 cm^{-1}) is indicative of turbostratic alignment (data not shown).[29] The ratio of the disorder induced D-peak (≈1350 cm^{-1}) to the first-order zone boundary phonon mode induced G peak (≈1580 cm^{-1}), namely the I_D/I_G, was 0.30 ± 0.08 whilst the I_{2D}/I_G = 0.75 ± 0.29 (2.33 eV). Raman mapping of the I_D/I_G ratio across entire apertures (≈8 × 10^3 μm^2) indicated that the graphene was approximately 1.6% monolayer and >98.2% bilayer, which was independently corroborated by contrast optical microscopy on Si/SiO_2 (300 nm) supported samples. Additional evidence for the number of layers in the CVD-synthesised graphene used herein is gleaned from further detailed Raman analysis. The blue-shift in the D, G, and 2D dispersion (52.0, 6.8, and 108.2 $cm^{-1}eV^{-1}$) strongly suggests a bilayer material, as substantiated by the findings in the literature.[30] Cross-sectional high resolution transmission electron microscopy independently confirmed the bilayer nature of the films evidencing a thickness of 0.73 nm (Figure 1g), whilst select-area electron diffraction hinted at turbostratic stacking with an inter-layer rotation of 11° (Figure 1f). The 1.95 eV 2D-peak was well-fitted with four-fold Lorentzians' (R^2 > 0.99) and showed a full-width at half-maximum of Γ_{2D} = 66.6 ± 1.5 cm^{-1}, hallmarks of Bernal-stacked bilayer graphene.[29,31,32] However, it has also been shown elsewhere[33] that two misoriented graphene layers exhibit a single 2D-peak around 2700 cm^{-1}, which we do indeed note at 2.33 eV and 2.71 eV. Thus, the bilayer graphene used herein is evidently macroscopically turbostratic with some Bernal-stacked regions, as one would come to expect from polycrystalline CVD-graphene. Transport studies gave a longitudinal resistivity of $\rho_{xx} \approx 4 \times 10^{-4}$ Ω cm, a charge carrier density $n_H \approx 5 \times 10^{12}$ cm^{-2}, and a Hall mobility of μ_H = 2000 cm^2 V^{-1} s^{-1}.

2.2. Electron Transparency of Multi-Layer CVD Graphene

The electron transparency of graphene has been the focus of much debate in recent literature.[25,26,34] Despite this few reports have detailed the electron transparency of CVD graphene.[35,36] Studies, most often performed in transmission electron microscopes employing mechanically exfoliated graphene, revealed that electrons accelerated to >100 keV irreversibly modify the crystallinity of the graphene via ablation, radiolysis, thermal

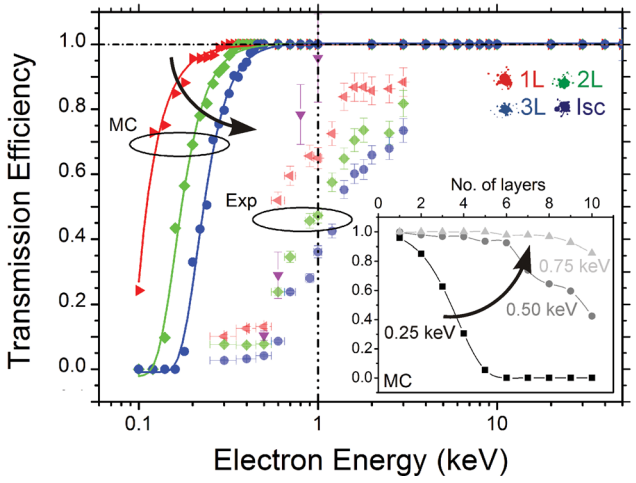

Figure 2. Electron transparency of chemical vapor deposited graphene. Absolute upper transmission boundaries as inferred from MC simulations depicting the variation in transmission efficiency for ideal graphene membranes as a function of layer number and electron energy. Sigmoidal fits and standard errors shown. Experimentally recorded electron transmission efficiency (Exp) is shown for chemical vapor deposited graphene, obtained by bright-field contrast electron microscopy with landing energies calibrated by angle-invariant specimen current (I_{sc}) electron microscopy. 1L denotes monolayer; 2L, bilayer; and 3L, trilayer CVD-graphene. Insert: Variation in transmission efficiency as a function of the number of graphene layers (0–10 layers) at 0.25 keV, 0.50 keV, and 0.75 keV.

diffusion, and radiation-induced diffusion.[37–39] Conversely, extremely low energy electrons (<0.1 keV) have been experimentally demonstrated, in low energy electron holography, to traverse membranes of graphene and various graphene-derivatives, such as graphene oxide and "ultrathin carbon", with efficiencies in excess of 73% for monolayer graphene, 55% for bilayer graphene, and 30% for trilayer graphene.[35,36,40,41] **Figure 2** shows Monte Carlo (MC) simulations and the measured electron transmission efficiency (η) for mono and multilayer graphene, that we have classically validated by:

$$I(d) = I_0 e^{-d/\lambda(E)} \quad (1)$$

where $I(d)$ is the transmission efficiency as a function of distance, d, I_0 is the initial beam intensity, and $\lambda(E)$ is the mean free path of an electron accelerated to a kinetic energy, E. The electronic inelastic mean free path in graphite is >1.0 nm for E > 0.5 keV, with an approximate penetration depth Δ (in μm), as indicated by the Kanaya-Okayama formalism:

$$\Delta = 0.0276 A E^{1.67} / Z^{0.86} \rho \quad (2)$$

where A is the atomic weight, ρ is the density, and Z is the atomic number. For graphitic carbon $\Delta \approx 9.8$ nm (A = 12.011 g $mole^{-1}$, Z = 6, ρ = 2.26 g cm^{-3}), which is equivalent to approximately 28 graphene layers. As shown in Figure 2, our models approximately 0.2 keV is required to penetrate pristine monolayer graphene with η > 95%, whereas around 0.2 (0.3) keV is required for pristine bi- (tri-) layer graphene to achieve $\eta \approx$ 70%. For clarity, the insert shows the variation in electron transmission with layer number at 0.25 keV, 0.50 keV, and 0.75 keV. For

$E > 1$ keV, η tends toward 100% for idealized graphitic materials of up to 10 layers. In practical field emission triodes, the gate voltage is typically several hundred to a few thousand volts.[42] Thus, triodes employing our hybrid gate electrodes can expect the emergent electrons to efficiently traverse the gate.

MC simulations are the ubiquity in electron trajectory and transmission simulation studies. However, in atomic-scale systems such simulations pragmatically represent an upper transmission limit. The Fermi wavelength of the emergent electron beam at 1 kV is ≈1.2 nm. This is comparable to the *c*–*c* lattice spacing (0.142 nm) and the inter-graphene spacing (0.335 nm), as well as the electric field screening length in graphite (1.2 nm).[27] MC simulations are implicitly random and take account only of the average carbon atom density. This limits their applicability where coherency plays an important role, such as multi-layered graphene materials where effects such as Fabry-Pérot interference are important. As such the 98.2% transmission indicated in our MC simulations is purely an indicative absolute upper limit. In reality the actual transmission will be somewhat lower. Indeed, the measured electron transmission indicates an electron transmission efficiency of 87%, 74%, and 66% for mono-, bi-, and tri-layer graphene at 2 keV (see Experimental Section). Possible sources of discrepancies between the model and measurements arise as the model fails to account for local variations in electron landing energy, local variations in the graphene work function, graphene grain boundaries, polycrystallinity, lattice defects and impurities/dopants, backscattered and secondary electron populations, spherical and chromic aberrations, and the effects of local charge trapping and other perturbations in the surface potential associated with contaminants. Moreover, the angle at which the primary electrons impinge upon the graphene has been shown to greatly affect the transmission efficiency, thus techniques invariant toward the angular dispersion of the impinging primary electron beam must be considered.[43,44] Consequently, specimen current electron microscopy (I_{sc}) was employed to independently corroborate our bright-field contrast scanning transmission electron microscopy findings, as shown in Figure 2 (see Experimental Section). Raman spectroscopy indicated mean sp^2 domains ≈41 nm in size.[45] These misoriented finite domains within discrete graphene grains (≈5 μm in size), and the interfaces with which they define, perturb the macroscopic electronic structure markedly and alter the electronic transport within, and normal to the basal plane. These scatter sites, typically in the form of lattice dislocations, have been shown to reduce the measured transmission efficiency dramatically and, rather strikingly, even enhance reflectivity in the basal plane.[46] Extension of this conjecture to an out-of-plane geometry, particularly at lower beam energies, are supported by direct comparison of microscopic crystalline graphene and our macroscopic polycrystalline CVD samples, which corroborates our simulations excellently.[45] As previously eluded to, the interaction between the primary electron beam and the graphene is strongly correlated with the incident angle.[44] Further transmission suppression may well occur due to corrugations and strain-relieving membrane buckling, both of which we have observed directly. Despite the comparatively high speculated areal density of such topological defects, compared to exfoliated samples, our CVD bilayer graphene gates maintain a high measured transmission efficiency of 50–60% at 1 kV, which is dramatically higher than conventional grid gate electrodes.

2.3. Graphene-Gated Triode Performance

A schematic of the field emission diode and triode experimental setup is given in **Figure 3**a (see Experimental Section). Briefly, a fixed anode voltage (V_a) attracts the emergent electrons which are liberated by the gate voltage (V_g) where the anode current (I_a) and gate current (I_g) are measured. Throughout, nominally equivalent triode geometries have been compared, one employing a conventional bare metal grid gate and the other our graphene hybrid gate. Note that earlier experiments confirmed that the screen-printed carbon nanotube electron emitter, employed herein, (see Experimental Section) was hysteresis-free and demonstrated negligible variation in anode current with ramp number (<3.2% at $V_g = 0.9$ kV) (see Supporting Information, Figure S1). Figure 3b shows I_a and I_g as a function of V_g for the graphene hybrid gate. Linearity in the Fowler-Nordheim (FN) plot of V_g–I_a and V_a–I_a suggests that electron emission can be efficiently stimulated by either the gate or anode. In typical operation the anode stimulates electron emission whilst the gate modulates the magnitude of the beam current. The hybrid nanocarbon triode showed an approximate turn-on voltage (defined as the voltage required to emit 100 nA) of 166 V, with an emission current of 2.0 mA at 2.7 V μm^{-1}. Data was well-fitted ($R^2 > 0.98$) to the FN relation:

$$I_a = V_g^2 \beta^2 \left(A * A/\Theta\delta^2\right) \exp\left(-B\Theta^{3/2}\delta/\beta V\right) \quad (3)$$

where the slowly varying dimensionless Nordheim elliptical functions have been neglected for brevity, Θ is the work function of the CNT emitter (5.0 eV), β is the field enhancement factor of the electron emitter, A^* is the effective emission area, δ is the constant gate–anode separation (=200 μm), and A and B are constants equal to $(e^3/8\pi h) = 1.54 \times 10^{-6}$ A eV V^{-2}, and $(8\pi/3eh)(2m)^{1/2} = 6.83 \times 10^9$ (eV)$^{-3/2}$V m^{-1}, respectively.

Graphene hybrid and conventional bare gates were compared in diode and triode modes. As shown in Figure 3c, the graphene hybrid achieved a stable anode current of 3 mA at $V_g = 1.0$ kV. Diode and triode modes showed nominally equivalent behavior for the graphene hybrid. In triode mode the bare grid required $V_g = 2.2$ kV to obtain an equivalent anode current. The non-uniformity in the electric field distribution of the bare gate resulted in a mean aperture electric field some 12% lower than that of the hybrid gate. This manifests as the deleterious increase in turn-on voltage for the bare gate.

The transconductance(g_m) under typical operation conditions ($V_a = 4$ kV) for the graphene hybrid triode, calculated by:

$$\langle g_m \rangle = \left\langle \partial I_a / \partial V_g \big|_{V_a = \text{const}} \right\rangle \quad (4)$$

was 7.5 μS, more than two orders of magnitude larger than the transconductance of similar triode devices based on spaghetti-like carbon nanotube field emitters with conventional bare gates.[10] The triode geometry showed a comparatively low perveance (P), calculated by:

Adv. Funct. Mater. **2013**,
DOI: 10.1002/adfm.201300322

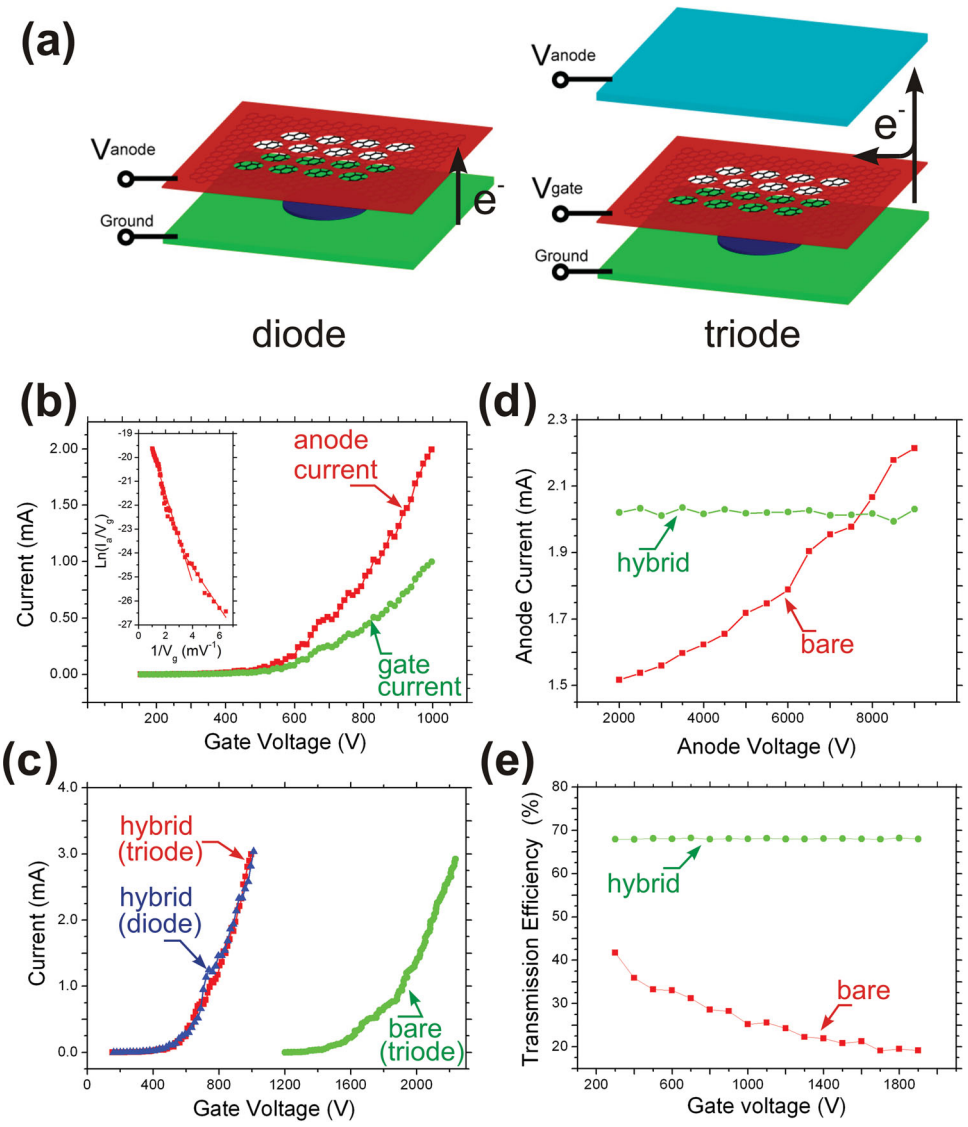

Figure 3. Field emission performance comparison of a bare conventional Mo gate and the hybrid graphene gate. a) Schematic of the experimental setup showing the diode (left) and triode (right) configurations. b) Hybrid gate performance in triode mode. Anode current and gate current as a function of gate voltage at V_a = 4 kV. c) The dependence of the anode current on gate voltage in diode and triode configurations for a bare and hybrid gate (V_a = 4 kV). d) Effect of anode voltage on anode current for a fixed gate voltage (V_g = 1 kV). e) Variation in transmission efficiency with gate voltage (V_a = 4 kV). Note the invariance in the transmission efficiency of the hybrid gate with gate voltage and anode current with anode voltage.

$$P = I_a V_a^{-3/2} \quad (5)$$

For the graphene gate the perveance was of the order of 0.03 μA $V^{-3/2}$, some 34% higher than the conventional gate but two-orders of magnitude less than commercially available emitters. This is a direct consequence of the triode geometry and CNT electron source morphology. The marked effect of V_a on I_a at fixed V_g (= 1 kV) for traditional bare gates is shown in Figure 3d. However, in the graphene hybrid triode, V_a had a negligible effect on I_a, which was only dependent on V_g. The triode output impedance (Z_0) of the bare gate triode, calculated by:

$$\langle Z_0 \rangle \cong \left\langle \partial V_a / \partial I_a |_{V_g = \text{const}} \right\rangle \quad (6)$$

was 14 MΩ, whilst that of the graphene hybrid was 70 MΩ. The amplification factor of the graphene triode was 524, which was ≈7.6 times larger than the amplification factor of the bare gate triode. At V_g = 1 kV, approximately 2 μA per aperture is sank in the gate, which when applying the Schottky formula for a non-Ohmic shot Noise limited electrode we find an upper bandwidth of around 6 GHz.

The dependency of the transmission efficiency (η) on V_g is shown in Figure 3e, where $\eta = I_a/(I_a + I_g)$, where I_a and I_g denote the anode and gate currents, respectively. For the bare gate the transmission efficiency decreased monotonically from around 40% to 20% with increasing V_g. In contrast, in the graphene hybrid the transmission was invariant with respect to V_g.

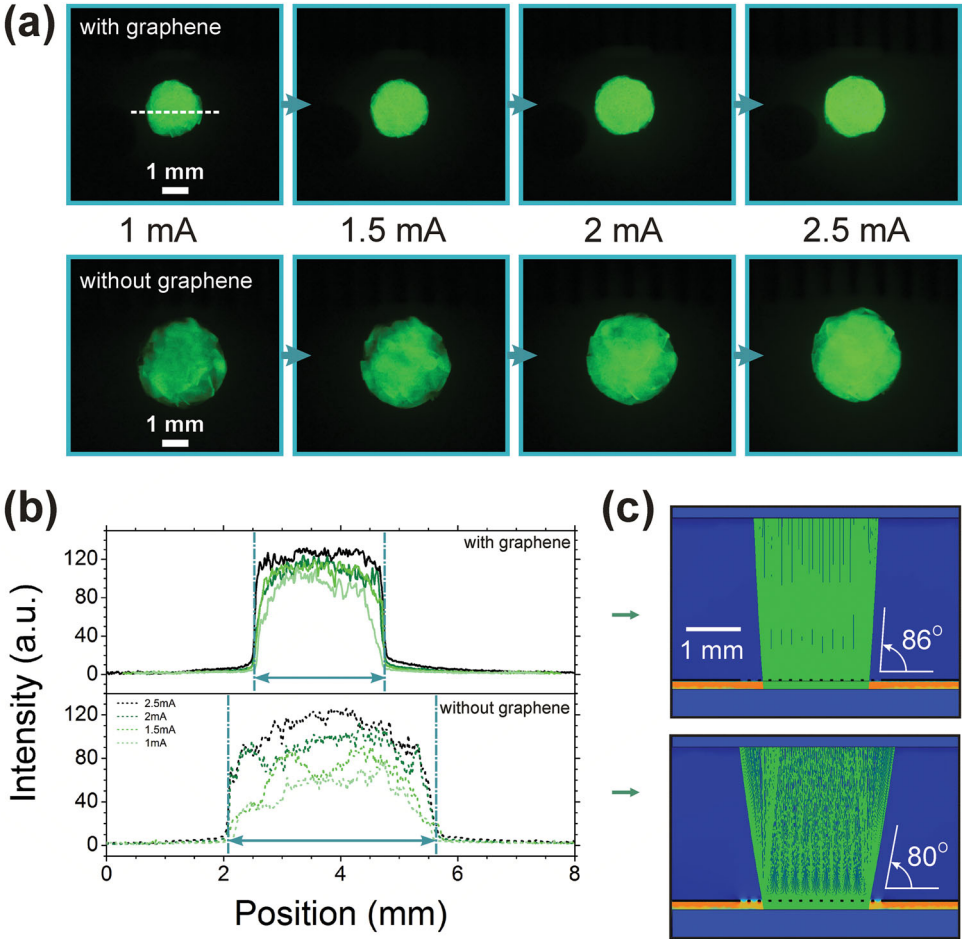

Figure 4. Electron beam uniformity. a) Integrated intensity images (ZnO: Zn) (triode configuration) operated at anode currents of 1 mA, 1.5 mA, 2 mA, and 2.5 mA showing enhanced uniformity in the graphene hybrid gate case (top) (scale bar: 2 mm). b) Integrated intensity cross-section showing narrower beam shape in the hybrid gate. Satellite peaks in the cross-section intensity map are due to anode imperfections. c) Simulated electron trajectories of the graphene hybrid and bare gates (scale bar: 1 mm). Empirical findings validate our ab-initio simulations well suggesting that the beam diameter of the graphene hybrid is between 63% (empirical) and 83% (theory) of an equivalent conventional bare gate. Modelling of the conventional gate indicated a beam divergence of approximately 80°, whilst the graphene hybrid showed a highly collimated 86° beam. Direct profile measurements showed a beam divergence of 76° for the conventional gate and 88° for the graphene hybrid, an improvement in beam collimation of some 86% due to graphene incorporation.

V_g defines the effective electron energy. Linearity of the V_g–I_a FN curve (insert in Figure 3b), for example, at V_g = 1 kV produces impinging electrons that are accelerated to around 1 keV giving an approximate transmission efficiency of the hybrid gate of ≈68%, some 30% lower than our theoretical predictions. However, the measured transmission efficiency was approximately equal to the grid porosity (70%) and showed extremely good correspondence with the measured transmission efficiency. The electron transmission model assumed free-standing, perfectly crystalline graphene and did not consider electron-opaque regions, such as the Mo grid. Normalizing to the occluded regions, we find an actual transmission efficiency of ≈97% confirming that the bulk of the electron population do indeed pass through the graphene rather than being captured by it. The finite pitch of the Mo grid limits the maximum attainable transmission. Thus, one possible approach in which to improve device performance would be to employ larger pitch grids to minimize the deleterious opaque regions. However, highly conductive graphene would be critical in this instance to ensure uniformity in the gate electric field. Notwithstanding, the measured transmission of graphene hybrid gate shows excellent consistency with earlier estimates and is greatly improved relative to the conventional bare gate.

To investigate the emitted beam characteristics, integrated intensity maps (ZnO: Zn phosphor) were acquired in a triode configuration at I_a = 1 mA, 1.5 mA, 2 mA, and 2.5 mA, as shown in **Figure 4**a. The diameter of the beam in the hybrid case is approximately 2.2 (±0.06) mm and was largely independent of V_g. The spot diameter for the traditional metal grid varied, non-uniformly between 2.8 mm and 3.4 mm. This severe dispersion is predominately attributed to the non-uniformity of the electric field distribution surrounding the bare

DOI: 10.1002/adfm.201300322

gate. The measured/modelled beam diameter for the hybrid gate was approximately 63%/58% that of the conventional bare gate (Figure 4b). Figure 4c depicts a cross-section of the electric field distribution with and without graphene (COMSOL Multi-physics V3.3A.), when V_g = 1 kV and V_a = 4 kV. The model suggests that the graphene planarises the metallic support, smoothing the electric field distribution ensuring a collimated beam. DC electrostatic models of the conventional metal gate indicated a beam divergence $\gamma = 80°$, whilst the graphene hybrid offered an increasingly collimated $\gamma = 86°$, where γ is defined as per Figure 4c. Measurements demonstrated a beam divergence of $\gamma = 76°$ for the conventional bare gate and $\gamma = 88°$ for the hybrid gate (where we note $\gamma_{ideal} = 90°$) due to graphene incorporation (Figure 4a). We attribute the remaining minor beam divergence to unavoidable Coulomb interactions. The hybrid gate showed an increasingly uniform electric field distribution (as the graphene passivated the electric field edge enhancement associated with the apertures periphery, which induced detrimental electron beam divergence) and a consequent collimated electron beam, both of which are critical in obtaining stable, high current densities for applications such as portable X-ray sources. A detailed study on a micro-focus nanocarbon micro-cathode X-ray source array employing an on-chip integrated graphene gate will be presented elsewhere.

At present, carbon derivatives, such as ion-textured graphite are widely adopted to coat field emission collectors and grid electrodes.[26] To investigate the comparative performance of our graphene hybrid gate to other available, low-cost carbon derivatives we considered commercially available 7 nm holey carbon grids as a disordered and discontinuous analogue to our crystalline graphene hybrid. The graphene hybrid gates offered similar emission improvements to the lacey carbon gates though the latter showed a marginally lower electron transparency, most likely attributed to the significantly thicker and more irregular films. Lacey carbon gates also showed a 3% higher turn-on voltage due to the reduced layer uniformity compared to the graphene. Moreover, the g_m of the lacey carbon grid was 49.3% lower than that of the graphene hybrid. Notwithstanding, perhaps the most notable difference was in emission stability. The lacey carbon gates were significantly less stable (±9.6%) compared to the graphene hybrid (±1.0%) for equivalent bias and time (V_g = 0.75 kV, V_a = 4 kV, t = 5.5 h) (see Supporting Information, Figure S2). Even under increasingly high driving biases, for example when V_g = 1.5 kV, the emission stability of the graphene hybrids was consistently < ±2.3%.

Figure 5a shows a typical accelerated lifetime test. For V_g < 1 kV, the emission variability (±1 S.D.) of the graphene hybrid triode was <2.2%. For V_g = 1.50 kV, 1.00 kV, and 0.75 kV, $<I_a>$ = 6.02 ± 0.05, 2.98 ± 0.03, and 1.03 ± 0.10 mA, respectively. Electron irradiation did not significantly degrade the graphene. Any induced defects would have manifest as instabilities in the emission current, with the emission becoming progressively stochastic. This was not the case. Scanning electron microscopy revealed that the graphene coverage prior to, and following a 5.5 h stability test performed at V_a = 3 kV and V_g = 1.5 kV, reduced the graphene coverage by only 17.4% (see Supporting Information, Figure S3), with no measureable alteration in the emission current. The observed defects are most likely transfer produced, however existing lattice interstitials, local plasma

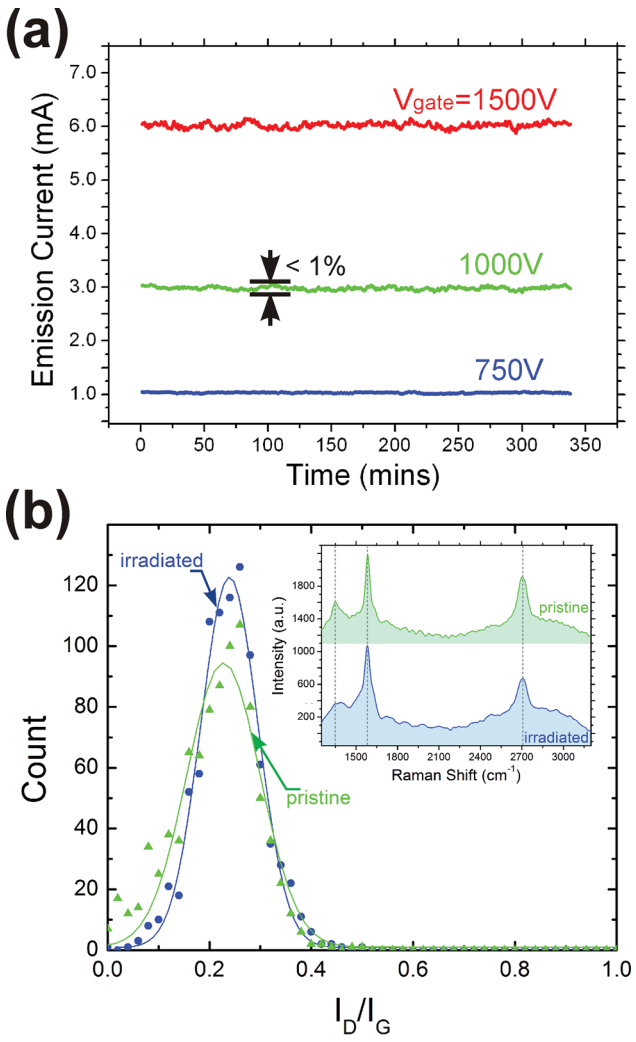

Figure 5. Gate stability. a) Room temperature accelerated lifetime measurement performed at 10^{-7} mbar (V_a = 4 kV, V_g = 1.5 kV, 1.0 kV, 0.75 kV). At gate biases ≤1 kV the emission shows variability (±1 S.D.) of <1.0% (V_g = 1 kV) and 2.2% (V_g = 1.5 kV). b) Graphene electron-beam resilience inferred by Raman spectroscopy. Gaussian fits to the I_D/I_G counts for pristine and irradiated samples acquired from more than 500 spectra. Insert: Example 2.33 eV Raman spectra of a pristine and irradiated sample.

stimulated vacancies, and radiation-induced chemical etching associated with chemisorbed species, may also have increased the rate of defect formation. No electron beam-induced formation of non-equilibrium graphitic nanostructures was noted, substantiating the resistance of graphene to the impinging beam.

Previous work has demonstrated the impressive resilience of graphene toward energetic impinging electrons of energies up to 86 keV, the knock-on damage threshold for sp^2 carbon.[34,39] This threshold is more than one order of magnitude greater than the typical operational potentials in standard triodes. In the case of graphene, scattering is coherent and elastically limited ensuring lattice thermalisation and negligible defect induction. Moreover, as graphitic nanocarbons have one of the lowest sputter cross-sections of any material (10^{-4}–10^{-1} barn),[25,47]

even high-defect-density graphene is an order of magnitude more robust than the ubiquitous transition metals employed in gate grid manufacture.[48] If we assume single monovacancy nucleation per nm^2, a typical operational beam current density (10^4–10^5 A cm^{-2})[49] is at least ten times less than the beam current density required to stimulate significant localised sputtering (≈10^6 A cm^{-2}). Raman spectroscopy performed on the graphene hybrid gates before (pristine) and after irradiation (irradiated) showed that the graphene was crystallographically unaffected by the impinging electron beam. More than 500 individual measurements were conducted on pristine and irradiated samples (2.33 eV) (Figure 5b). Negligible crystallographic variation between the two was noted. For the pristine samples, $<I_D/I_G>_{pristine} \approx 0.25$, whilst for the irradiated $<I_D/I_G>_{irradiated} \approx 0.26$. Representative Raman spectra from a pristine and irradiated sample are shown in the insert of Figure 5b.

3. Conclusions

Herein, we have presented, for the first time, a graphene hybrid gate electrode in a triode field emitter electron source. Conductive, electron transparent gate electrodes were fabricated from bilayer turbostratic graphene transferred to Mo grids and integrated into nanocarbon micro-triodes. Experimentally validated simulations showed that electrons with energies >1 keV efficiently (>95%) penetrate multi-layer graphene membranes. The graphene hybrid gates were shown to reduce the gate driving voltage by 1.1 kV due to the increased uniformity in the gate electric field distribution. The measured electron transmission efficiency of the gate electrode increased from 20% to 68% as a result of graphene incorporation, resulting in a triode amplification factor 7.6 times larger than devices based on conventional refractory metal grid gates. Integrated intensity images showed that the electron beam angular dispersion was improved by 12.3° relative to the uncoated gates, resulting in a 63% reduction in beam diameter. Negligible damage to the graphene was noted after lifetime tests with triodes demonstrating excellent stability (<2.2% over 5.5 h) all of which are critical device parameters required to achieve truly portable and inexpensive field emission electron sources.

4. Experimental Section

Graphene and Carbon Nanotube Chemical Vapor Deposition: Graphene was synthesised by hot-walled thermal chemical vapor deposition (CVD), as similarly reported in detail elsewhere.[13] Briefly, 5 sccm CH_4 (Air Products, 99.5%) was introduced to a 500-nm-thick physical vapor deposited Cu (and Ni) catalyst on 200 nm thermally oxidised Si, at 1000 °C in an Ar: H_2 ballast (960 (99.9997%): 40 (99.9992%) sccm, Air Products) at 25 mbar. Following the growth phase samples where quenched using 2000 sccm N_2 (99.99%, Air Products) to 250 °C prior to system venting. Mono-, bi-, and tri-layer graphene was grown by Cu and Ni-catalyzed CVD under equivalent growth conditions.

Purified, thermal CVD-synthesised multi-walled carbon nanotubes (MWCNTs) were purchased from XFNANO Materials Tech. Co. and had a CNT content > 95%. The as-purchased MWCNTs had an inner/outer diameter of <3/8 nm and were 10–30 μm in length.

Material Characterization: Graphene was optically characterised using an Hitachi U-4100 UV-Vis-NIR spectrophotometer operated in transmission mode at STP. Raman analysis was performed using an InVia Raman spectrometer operated at 2.71 eV (457 nm, Ar), 2.33 eV (532 nm, diode), and 1.96 eV (633 nm, He-Ne) with an incident power <10 mW fitted a linear piezo xy stage (min. step = 0.2 μm) operated over triplicate accumulations with the graphene supported on rectangular TEM grids. The sample topography was inspected using a Carl Zeiss Gemini and a FEI Quanta 20 scanning electron microscope. High resolution transmission electron micrographs and select area electron diffraction patterns were acquired using a JEOL JEM-4000EX operated at 80 keV with a current density <20 pA cm^{-2}. Electrical conductivity, resistivity, and charge carrier density measurements were conducted in a Hall MMR system operated at STP. A 50 μm × 50 μm standard four-terminal van der Pauw configuration was patterned by electron beam lithography (Nanobeam Ltd.) and oxygen reactive ion etching (Philips – 50 W, 0.1 mbar, 20 s), with Ti/Au (15/60 nm) contacts thermally evaporated (Lesker PVD 75) on the Si/SiO_2 (300 nm) supported samples.

Graphene Gate and Carbon Nanotube Electron Emitter Fabrication: Graphene hybrid gates were fabricated by transferring CVD-grown graphene to Mo grids (Zhong Jing Ke Yi Ltd.) via standard $FeCl_3$–H_2O (25 wt%) wet-etching of the underlying catalyst using a 100 nm spin-coated PMMA mediator, as reported in more detail elsewhere.[50] PMMA/graphene was transferred from the etchant solution to a de-ionised water bath and floated onto Mo grids. PMMA was removed with repeated acetone dips and finally rinsed in isopropanol. Mo was selected over conventional Cu transmission electron microscopy grids because of its low backscatter electron yield η^* (for 1 keV incident primary electrons: $\eta^*_{Mo} = 0.2$, $\eta^*_{Cu} = 0.3$–0.5),[51–53] low secondary electron yield γ (for 1 keV incident primary electrons: $\gamma_{Mo} = 0.7$, $\gamma_{Cu} = 1.4$–1.7),[54,55] and its high mechanical rigidity. Various grid apertures (50, 100, 150, 200 μm) with a transmissions ratio of 70% were investigated. For apertures >150 μm graphene coverage was poor, whilst 100 μm apertures offered optimal transfer with minimised pin holes at maximum aperture.

As-purchased MWCNTs were purified via chemical oxidation using of $K_2Cr_2O_7$, as detailed in our previous work.[56] Purified MWCNTs were mixed with ethylcellulose and terpineol and agitated at 70 °C for 1 h. Once cooled the MWCNT slurry was screen-printed onto 50 ± 0.2 μm Mo foil through a 350 pitch mesh. Pastes had a typical CNT concentration of ≈5%. Emitters were left at STP to dry and then heated to 400 °C in a sinter furnace to remove residual organics.

Electron Transparency: The electron transparency of graphene was determined using two-dimensional MC electron trajectory software (Casino v3.2). Individual graphene layers were assumed turbostratic, graphitic in material constants, incommensurate, and to be 0.34 nm thick. The electron transparency was empirically evaluated by bright field contrast electron microscopy using a field emission Hitachi S-5500 scanning transmission electron microscope (STEM) with a 200 μm diameter probe diameter operated in bright field mode with a current density <1 A cm^{-2}. The finite size of the bright field detector and the non-collimated electron beam in typical STEM systems induced errors in the measured transmission spectra. Indeed, the elastically dominated electron-lattice interactions for the graphene gate will result in large scatter angles. Thus, electrons impinging on the bright field detector are sourced from a variety of positions angles and some transmitted electrons may certainly be deflected outside the extent of the detector.[57] As a result the landing energy of the contrast measurements was independently calibrated by direct specimen current imaging electron microscopy,[58] which is insensitive to the electron trajectories, using a Zeiss Sigma scanning electron microscope with integrated pico-ammeter operated from 0.3–3.0 keV. The specimen current (I_{SC}) relates to the transmitted electron current (I_{TE}), the primary electron current (I_{PE}), the backscattered electron current (I_{BSE}), and the secondary electron current (I_{SE}) by; $I_{TE} = (I_{PE} - I_{BSE} - I_{SE} - I_{SC}) = [I_{PE}\ (1 - \eta - \delta) - I_{SC}]$, as $I_{BSE} = \eta^* I_{PE}$, and $I_{SE} = \delta I_{PE}$, where η^* is the backscatter electron yield, and δ is the secondary electron yield, both of which are dependent on the landing energy of the primary electrons and have been estimated from literature based on cleaved high purity pyrolytic graphite.[59]

Adv. Funct. Mater. 2013,
DOI: 10.1002/adfm.201300322

Field Emission Measurement: Field emission measurements were conducted in two custom-built, ultra-high vacuum (UHV) systems that were turbo molecular and ion pumped to base pressures of $<10^{-9}$ mbar at room temperature. Samples were heated in UHV conditions to 200 °C for 24 h to remove water vapor and other absorbates and allowed to naturally cool to room temperature. A 2 mm diameter and 10 µm thick screen-printed thin film of chemical vapor deposited multi-walled carbon nanotubes on Mo foil formed the cathode, adjacent to the graphene gate, which was grounded. In diode mode, we adopted a parallel-plate set up with a cathode-anode distance of 3 mm defined mechanically by clamped alumina spacers. In triode mode, the gate-cathode distance was 200 µm with an anode-gate distance of 3 mm, again mechanically clamped with alumina spacers. The anode was positively biased using an automated LabView controlled variable DC voltage supply. The anode current was measured using a Keithley 485 picoammeter, fitted with a 100 kΩ ballast resistance and attached to a computerised data acquisition system. The gate voltage was controlled by a secondary, custom-built source measure unit. Integrated intensity maps were captured using a chamber mounted CCD. Beam profiles were assessed by comparing image grey scale intensities for triodes with traditional metal gates and graphene hybrid gates.

<> denotes mean values, with all errors quoted as ± 1 standard deviation (S.D.).

Supporting Information

Supporting Information is available from the Wiley Online Library or from the author.

Acknowledgements

C.L. and M.T.C. contributed equally to this work. This work is supported by supported by National Key Basic Research Program 973(2010CB327705), National Natural Science Foundation Project (51202027, 51120125001), China Postdoctoral Science Foundation funded project (2012M511648, 2013T60489), Foundation of Doctoral Program of Ministry of Education (20100092110015), and the Research Fund for International Young Scientists from NSFC (51050110142). The Authors' thank the Cavendish Laboratory, Cambridge University for the kind use of their Raman and electron microscopy facilities. M.T.C. acknowledges the Winston Churchill Trust and the Isaac Newton Trust, Trinity College Cambridge University, for generous financial support.

Received: January 27, 2013
Revised: June 20, 2013
Published online:

[1] W. A. De Heer, A. Châtelain, D. Ugarte, *Science* **1995**, *270*, 5239.
[2] K. B. K. Teo, M. Chhowalla, G. A. J. Amaratunga, W. I. Milne, G. Pirio, P. Legagneux, F. Wyczisk, D. Pribat, D. G. Hasko, *Appl. Phys. Lett.* **2002**, *80*, 11.
[3] W. Wei, K. Jiang, Y. Wei, P. Liu, K. Liu, L. Zhang, Q. Li, S. Fan, *Appl. Phys. Lett.* **2006**, *89*, 20.
[4] R. H. Baughman, A. A. Zakhidov, W. A. de Heer, *Science* **2002**, *297*, 5582.
[5] Z. Liu, G. Yang, Y. Z. Lee, D. Bordelon, J. Lu, O. Zhou, *Appl. Phys. Lett.* **2006**, *89*, 10.
[6] J. Zhang, G. Yang, Y. Cheng, B. Gao, Q. Qiu, Y. Z. Lee, J. P. Lu, O. Zhou, *Appl. Phys. Lett.* **2005**, *86*, 18.
[7] W. I. Milne, K. B. K. Teo, G. A. J. Amaratunga, P. Legagneux, L. Gangloff, J. P. Schnell, V. Semet, V. T. Binh, O. Groening, *J. Mater. Chem.* **2004**, *14*, 6.
[8] W. I. Milne, K. B. K. Teo, M. Mann, I. Y. Y. Bu, G. A. J. Amaratunga, N. De Jonge, M. Allioux, J. T. Oostveen, P. Legagneux, E. Minoux, L. Gangloff, L. Hudanski, J. P. Schnell, L. D. Dieumegard, F. Peauger, T. Wells, M. El-Gomati, *Phys. Status Solidi A* **2006**, *203*, 6.
[9] Y. Saito, S. Uemura, *Carbon* **2000**, *38*, 2.
[10] Y. M. Wong, W. P. Kang, J. L. Davidson, W. Hofmeister, S. Wei, J. H. Huang, *Diam. Relat. Mater.* **2005**, *14*, 3.
[11] F. Torrisi, T. Hasan, W. Wu, Z. Sun, A. Lombardo, T. S. Kulmala, G.-W. Hsieh, S. Jung, F. Bonaccorso, P. J. Paul, D. Chu, A. C. Ferrari, *ACS Nano* **2012**, *6*, 4.
[12] S. Hertel, D. Waldmann, J. Jobst, A. Albert, M. Albrecht, S. Reshanov, A. Schöner, M. Krieger, H. B. Weber, *Nat. Commun.* **2012**, *3*.
[13] S. Bae, H. Kim, Y. Lee, X. F. Xu, J. S. Park, Y. Zheng, J. Balakrishnan, T. Lei, H. R. Kim, Y. I. Song, Y. J. Kim, K. S. Kim, B. Ozyilmaz, J. H. Ahn, B. H. Hong, S. Iijima, *Nat. Nanotechnol.* **2010**, *5*, 8.
[14] K. Keun Soo, Z. Yue, J. Houk, L. Sang Yoon, K. Jong Min, K. S. Kim, A. Jong-Hyun, P. Kim, C. Jae-Young, H. Byung Hee, *Nature* **2009**, *457*, 7230.
[15] I. Diez-Perez, Z. Li, J. Hihath, J. Li, C. Zhang, X. Yang, L. Zang, Y. Dai, X. Feng, K. Muellen, N. Tao, *Nat. Commun.* **2010**, *1*, 31.
[16] F. Schwierz, *Nat. Nanotechnol.* **2010**, *5*, 7.
[17] M. Qian, T. Feng, H. Ding, L. Lin, H. Li, Y. Chen, Z. Sun, *Nanotechnology* **2009**, *20*, 42.
[18] C.-K. Huang, Y. Ou, Y. Bie, Q. Zhao, D. Yu, *Appl. Phys. Lett.* **2011**, *98*, 26.
[19] J.-H. Chen, C. Jang, S. Xiao, M. Ishigami, M. S. Fuhrer, *Nat. Nanotechnol.* **2008**, *3*, 4.
[20] X. Li, G. Zhang, X. Bai, X. Sun, X. Wang, E. Wang, H. Dai, *Nat. Nanotechnol.* **2008**, *3*, 9.
[21] A. K. Geim, *Science* **2009**, *324*, 5934.
[22] L. Xuesong, C. Weiwei, A. Jinho, K. Seyoung, N. Junghyo, Y. Dongxing, R. Piner, A. Velamakanni, J. Inhwa, E. Tutuc, S. K. Banerjee, L. Colombo, R. S. Ruoff, *Science* **2009**, *324*, 5932.
[23] R. R. Nair, P. Blake, A. N. Grigorenko, K. S. Novoselov, T. J. Booth, T. Stauber, N. M. R. Peres, A. K. Geim, *Science* **2008**, *320*, 5881.
[24] J. W. Suk, A. Kitt, C. W. Magnuson, Y. Hao, S. Ahmed, J. An, A. K. Swan, B. B. Goldberg, R. S. Ruoff, *ACS Nano* **2011**, *5*, 9.
[25] A. W. Robertson, C. S. Allen, Y. A. Wu, K. He, J. Olivier, J. Neethling, A. I. Kirkland, J. H. Warner, *Nat. Commun.* **2012**, *3*, 1144.
[26] J. Luo, P. Tian, C.-T. Pan, A. W. Robertson, J. H. Warner, E. W. Hill, G. A. D. Briggs, *ACS Nano* **2011**, *5*, 2.
[27] H. Miyazaki, S. Odaka, T. Sato, S. Tanaka, H. Goto, A. Kanda, K. Tsukagoshi, Y. Ootuka, Y. Aoyagi, *Appl. Phys. Exp.* **2008**, *1*, 3.
[28] K. F. Mak, M. Y. Sfeir, Y. Wu, C. H. Lui, J. A. Misewich, T. F. Heinz, *Phys. Rev. Lett.* **2008**, *101*, 19.
[29] L. M. Malard, M. A. Pimenta, G. Dresselhaus, M. S. Dresselhaus, *Phys. Rep.* **2009**, *473*, 5.
[30] R. Rao, D. Tishler, J. Katoch, M. Ishigami, *Phys. Rev. B* **2011**, *84*, 11.
[31] R. Saito, M. Hofmann, G. Dresselhaus, A. Jorio, M. S. Dresselhaus, *Adv. Phys.* **2011**, *60*, 3.
[32] A. C. Ferrari, J. C. Meyer, V. Scardaci, C. Casiraghi, M. Lazzeri, F. Mauri, S. Piscanec, D. Jiang, K. S. Novoselov, S. Roth, A. K. Geim, *Phys. Rev. Lett.* **2006**, *97*, 18.
[33] P. Poncharal, A. Ayari, T. Michel, J. L. Sauvajol, *Phys. Rev. B* **2008**, *78*, 11.
[34] F. Börrnert, S. M. Avdoshenko, A. Bachmatiuk, I. Ibrahim, B. Büchner, G. Cuniberti, M. H. Rümmeli, *Adv. Mater.* **2012**, *24*, 41.
[35] J. Y. Mutus, L. Livadaru, J. T. Robinson, R. Urban, M. H. Salomons, M. Cloutier, R. A. Wolkow, *New J. Phys.* **2011**, *13*.
[36] J.-N. Longchamp, T. Latychevskaia, C. Escher, H.-W. Fink, *Appl. Phys. Lett.* **2012**, *101*, 11.
[37] K. Urban, A. Seeger, *Philos. Mag.* **1974**, *30*, 6.
[38] R. F. Egerton, P. Li, M. Malac, *Micron* **2004**, *35*, 6.

[39] F. Banhart, *Rep. Prog. Phys.* **1999**, *62*, 8.
[40] D. Rhinow, M. Büenfeld, N.-E. Weber, A. Beyer, A. Gölzhäuser, W. Kühlbrandt, N. Hampp, A. Turchanin, *Ultramicroscopy* **2011**, *111*, 5.
[41] I. Muellerova, M. Hovorka, R. Hanzlikova, L. Frank, *Mater. Transactions* **2010**, *51*, 2.
[42] W. A. de Heer, J.-M. Bonard, K. Fauth, A. Châtelain, D. Ugarte, L. Forró, *Adv. Mater.* **1997**, *9*, 1.
[43] M. H. Gass, U. Bangert, A. L. Bleloch, P. Wang, R. R. Nair, A. K. Geim, *Nat. Nanotechnol.* **2008**, *3*, 11.
[44] J. C. Meyer, A. K. Geim, M. I. Katsnelson, K. S. Novoselov, T. J. Booth, S. Roth, *Nature* **2007**, *446*, 7131.
[45] M. M. Lucchese, F. Stavale, E. H. M. Ferreira, C. Vilani, M. V. O. Moutinho, R. B. Capaz, C. A. Achete, A. Jorio, *Carbon* **2010**, *48*, 5.
[46] O. V. Yazyev, S. G. Louie, *Nat. Mater.* **2010**, *9*, 10.
[47] J. C. Meyer, F. Eder, S. Kurasch, V. Skakalova, J. Kotakoski, H. J. Park, S. Roth, A. Chuvilin, S. Eyhusen, G. Benner, A. V. Krasheninnikov, U. Kaiser, *Phys. Rev. Lett.* **2012**, *108*, 19.
[48] R. F. Egerton, R. McLeod, F. Wang, M. Malac, *Ultramicroscopy* **2010**, *110*, 8.
[49] E. Minoux, O. Greening, K. B. K. Teo, S. H. Dalai, L. Gangloff, J. P. Schnell, L. Hudanski, I. Y. Y. Bu, P. Vincent, P. Legagneux, G. A. J. Amaratunga, W. I. Milne, *Nano Lett.* **2005**, *5*, 11.
[50] J. Sun, N. Lindvall, M. T. Cole, K. T. T. Angel, T. Wang, K. B. K. Teo, D. H. C. Chua, J. Liu, A. Yurgens, *IEEE. T. Nanotechnol.* **2011**, *1*, 1.
[51] E. J. Sternglass, *Phys. Rev.* **1954**, *95*, 2.
[52] K. Goto, K. Ishikawa, T. Koshikawa, R. Shimizu, *Surf. Sci.* **1975**, *47*, 2.
[53] Z. J. Ding, R. Shimizu, *Scanning* **1996**, *18*, 2.
[54] D. C. Joy, *Scanning* **1995**, *17*, 5.
[55] L. Yinghong, D. C. Joy, *Surf. Interface Anal.* **2005**, *37*, 11.
[56] J. T. Li, W. Lei, X. B. Zhang, X. D. Zhou, Q. L. Wang, Y. N. Zhang, B. P. Wang, *Appl. Surf. Sci.* **2003**, *220*, 1.
[57] H. Farhang, E. Napchan, B. H. Blott, *J. Phys. D* **1993**, *26*, 12.
[58] D. E. Newbury, ITTRI, Chicago **1976**.
[59] N. R. Whetten, *J. Appl. Phys.* **1963**, *34*, 4.

Adv. Funct. Mater. **2013**,
DOI: 10.1002/adfm.201300322